Localized analysis of satellite tracking data for studying time-variable Earth's gravity fields

Shin-Chan Han,[1,2] David D. Rowlands,[1] Scott B. Luthcke,[1] and Frank G. Lemoine[1]

Received 6 August 2007; revised 12 November 2007; accepted 2 January 2008; published 4 June 2008.

[1] We present a method to analyze the observations of relative distance change between two low Earth orbiting satellites of the Gravity Recovery And Climate Experiment (GRACE) mission after removing the effects caused by the mean gravity field and better-known temporal mass redistribution. The gravitational acceleration exerted by the block mean mass within a region on the Earth surface is formulated by point mass approximation and by spherical harmonic expansion. In addition to the regional mass parameters, the arc-dependent parameters (initial relative state vectors) is simultaneously modeled to remove the signals not associated with the mass variation within the focus area. While a certain level of approximation, that is committed when locally formulating the gravitational acceleration vector for numerical integration, causes model error, we benefit from regionally estimating time-variable mass with improved spatial and temporal resolutions. In addition, various temporal parameterizations depending on geographical areas and expected signals can be applied for the regional analysis in a straightforward manner and it helps to retrieve even sub-daily time-variable signals such as tides from many years of GRACE data. We present the results of hydrology and ocean tide recovery in South America, Africa, North America, and Antarctica from the analysis of 3.5 years of GRACE tracking data and compare them with the traditional global harmonic approach. The algorithm development thoroughly described here will be helpful for the science community to exploit fundamental data (range rate) of the GRACE mission in addition to monthly gravity products.

Citation: Han, S.-C., D. D. Rowlands, S. B. Luthcke, and F. G. Lemoine (2008), Localized analysis of satellite tracking data for studying time-variable Earth's gravity fields, *J. Geophys. Res.*, *113*, B06401, doi:10.1029/2007JB005218.

1. Introduction

[2] The mass fluxes, transports, and adjustments within the Earth system are manifested in the temporal changes of the Earth's gravity field. The large-scale mass variations, which the Gravity Recovery and Climate Experiment (GRACE) satellites have been observing since their launch in 2002, show spatially and temporally distinctive patterns in every region because they originate from dissimilar physical sources. The largest variability is being observed from GRACE over the continents due to the terrestrial water storage variations with dominantly seasonal periodicity [*Tapley et al.*, 2004a]. It is due to the fact that the mass variations caused by the atmosphere, tides (solid Earth, ocean, and pole), and barotropic ocean usually have been modeled a priori and removed from the GRACE observations [*Bettadpur*, 2004] to construct a monthly mean gravity field, and consequently most of the signals comprise the "full" effect of terrestrial water storage on the continents [*Tapley et al.*, 2004a]. However, it is expected that these signals also contain "residuals" with respect to the applied models for the ocean tides (especially over the polar regions) and the atmosphere and ocean mass, but with magnitudes smaller than the primary hydrology signal and at various temporal frequencies. Each of the time-variable signals appears only associated with its own particular geographical area and usually has characteristic temporal behavior and intensity.

[3] The global spherical harmonic analysis of the GRACE satellite-to-satellite tracking (SST) data has been the principal approach to generate monthly mean geopotential fields. The temporal variations of the geophysical and climate signals are typically derived from the time series of spherical harmonic coefficients representing the monthly mean gravity field. Some various spatial smoothing techniques developed to optimally mitigate the ill-determined higher degree and order coefficients such as *Wahr et al.* [1998], *Davis et al.* [2004], *Han et al.* [2005a] and *Swenson and Wahr* [2006] are applied to study hydrological mass fluxes in large river basins [*Tapley et al.*, 2004a], ice sheet

[1]Planetary Geodynamics Laboratory, NASA Goddard Space Flight Center, Greenbelt, Maryland, USA.
[2]Goddard Earth Science and Technology Center, University of Maryland Baltimore County, Baltimore, Maryland, USA.

Copyright 2008 by the American Geophysical Union.
0148-0227/08/2007JB005218$09.00

mean mass fluxes [*Velicogna and Wahr*, 2006], and ocean mass variations [*Chambers et al.*, 2004; *Zlotnicki et al.*, 2007]. However, the distinct regional characteristic of each temporal mass variation due to various physical reasons is a natural motivation to seek better methods to quantify such regional variations. Moreover, the systematic (correlated) error associated with the incomplete modeling of relatively well-known mass variations (tides, non-tidal atmosphere and ocean mass, etc) has been reported to be problematic especially in the resonant orders in the monthly mean spherical harmonics [*Han et al.*, 2004]. Significant degradation of the monthly gravity harmonic solutions has been reported by *Wagner et al.* [2006], due to sparse repeat tracks of 61/4 (rev/day) of the GRACE orbits in deep resonance. Instead of solving individual harmonic coefficient, *Rowlands et al.* [2005] tried to estimate the linear-combined (lumped) coefficients (called mascon). This method inherently uses constraints among the coefficients that are dependent on geographic locations. *Han et al.* [2005b] used downward-continuation of the in situ geopotential difference that is pre-determined from the satellite tracking data analysis. Both methods demonstrated enhancement of the solutions (temporally and spatially) for recovering the time-variable (regional) gravity fields. *Rowlands et al.* [2002] and *Mayer-Gürr et al.* [2006] also present the global gravity field analysis using short-arc length (such as 15 min) of the low-low satellite tracking data (which are only available from GRACE mission currently).

[4] In this study, we present an end-to-end algorithm developed to mitigate inefficacy in global spherical harmonic analysis and to optimally process the GRACE K-Band Range Rate (KBRR) data for estimation of regionally characterized mass variation, on the basis of the orbital state vector integration from the local formulation of the gravitational acceleration. The KBR instrument measures the mean gravity field and time-variable mass distribution through the effect of these parameters on the satellite orbits. Minute changes in KBRR data (±2 μm/s) due to temporal mass variation are being measured by the onboard instrument with an accuracy of 0.2–0.3 μm/s (inferred from the post-fit residuals). Our approach first removes the mean gravity effect from the KBRR measurements (±2 m/s, which is mostly due to the Earth's oblateness). From years of GRACE data, the spherical harmonic representation has been used successfully to model the mean geopotential field with a 100-fold improvement (over limited spectral bands) [*Tapley et al.*, 2004b]. Using such a reference gravity model (in the form of spherical harmonic coefficients), we determine the precise satellite orbits and calculate range-rates which are then removed from the raw range-rate measurements. The orbits we need should account for the steady state gravity field, instantaneous mass variation caused by some of the better-known gravitational forces such as tides, and non-conservative forces like air drag. We do not want to have the orbits affected by the instantaneous gravity forces we are seeking for such as terrestrial water mass, ice mass, earthquake, and so on. We describe the details of orbit processing algorithm satisfying this condition in section 3. After reducing the measurements based on the aforementioned orbital trajectory, the remaining residual range-rate (that is highly non-stationary over the globe) is our primary observation to model the temporal mass variation over the region. In section 2, we discuss the detailed algorithm on how to process the residual range-rate data and the basis function used for modeling the mass variation on the surface. In section 3, we present some examples such as hydrology and tide recovery in the various regions including South America, Africa, North America and Antarctica. Finally we summarize the current work and present perspectives about future opportunities in section 4.

2. Method

[5] We start this section by developing the observational equation relating the range-rate measurement, which is a non-linear function of the orbital state vector, and the source parameter, which is the time-variable mass on the Earth's surface. All vectors used in the derivations are parameterized in a non-rotating inertial coordinate system. We examine approximation error associated with mass parameterization and discuss analytic formulation of the temporal variations, especially designed for estimating high-frequency (sub-daily and daily) mass variation such as tides. Finally we show how we handle the effect caused by surface mass load.

2.1. Observation Equation

[6] The orbital state vectors including the position $\mathbf{r}(t)$ and velocity $\mathbf{v}(t)$ of a satellite at time t can be calculated by integrating the velocity and acceleration vectors over time period $t-t_0$ as follows:

$$\mathbf{r}(t) = \mathbf{r}(t_0) + \int_{t_0}^{t} \mathbf{v}(t')dt', \tag{1}$$

$$\mathbf{v}(t) = \mathbf{v}(t_0) + \int_{t_0}^{t} \mathbf{a}(t')dt', \tag{2}$$

where the initial state is $\mathbf{r}(t_0)$ and $\mathbf{v}(t_0)$. The introduced acceleration vector $\mathbf{a}(t)$ is decomposed into two components as follows:

$$\mathbf{a}(t) = \tilde{\mathbf{a}}(t) + \delta\mathbf{a}(t), \tag{3}$$

where $\tilde{\mathbf{a}}(t)$ is the calculated acceleration vector (i.e., from a priori gravitational potential model and other force models) and $\delta\mathbf{a}(t)$ represents the acceleration caused by the mismodeled and un-modeled temporal changes (e.g., surface mass variation including hydrology, ice mass change, solid-Earth deformation, remaining ocean tide and atmosphere, etc). Certainly the time variable gravitational acceleration $\delta\mathbf{a}(t)$ attracting the satellites would be regionally intense due to non-stationary distribution of the surface mass variation on the globe with peculiar frequencies (from seasonal for hydrology to once and twice per day for ocean tide). By putting (3) into (1) and (2), we express the position and

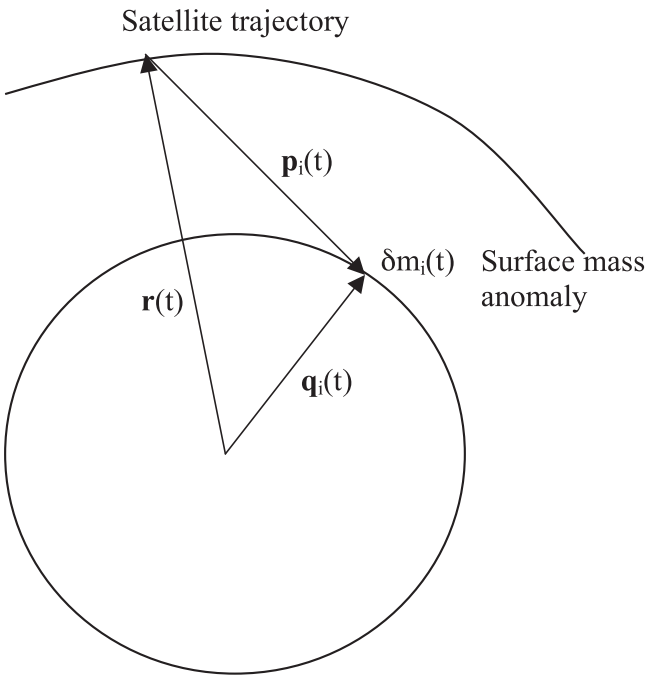

Figure 1. A schematic diagram highlighting the vectors defined in the section 2.1.

velocity vectors in terms of un-modeled surface mass attraction as follows:

$$\mathbf{r}(t) = \tilde{\mathbf{r}}(t) + \delta\mathbf{r}^0 + \int_{t_0}^{t}\int_{t_0}^{t'} \delta\mathbf{a}(t'')dt''dt', \tag{4}$$

$$\mathbf{v}(t) = \tilde{\mathbf{v}}(t) + \delta\mathbf{v}^0 + \int_{t_0}^{t} \delta\mathbf{a}(t')dt', \tag{5}$$

where $\tilde{\mathbf{r}}(t)$ and $\tilde{\mathbf{v}}(t)$ are the calculated position and velocity vectors obtained by integrating $\tilde{\mathbf{a}}(t)$. $\delta\mathbf{r}^0$ and $\delta\mathbf{v}^0$ are "incremental" initial state vector indicating deviation of the true position and velocity vectors from the calculated ones, respectively, at the initial epoch t_0.

[7] The inter-satellite tracking measurements such as the range $\rho(t)$ and range-rate $\dot{\rho}(t)$ between two satellites are formulated in terms of inter-satellite state vectors as follows:

$$\rho(t) = \sqrt{\mathbf{r}_{12}(t)^T\mathbf{r}_{12}(t)}, \tag{6}$$

$$\dot{\rho}(t) = \mathbf{v}_{12}(t)^T\mathbf{r}_{12}(t)/\sqrt{\mathbf{r}_{12}(t)^T\mathbf{r}_{12}(t)}, \tag{7}$$

where the inter-satellite position and velocity vectors are given as follows:

$$\mathbf{r}_{12}(t) = \mathbf{r}_1(t) - \mathbf{r}_2(t) = \tilde{\mathbf{r}}_{12}(t) + \delta\mathbf{r}_{12}^0 + \int_{t_0}^{t}\int_{t_0}^{t'} \delta\mathbf{a}_{12}(t'')dt''dt', \tag{8a}$$

$$\mathbf{v}_{12}(t) = \mathbf{v}_1(t) - \mathbf{v}_2(t) = \tilde{\mathbf{v}}_{12}(t) + \delta\mathbf{v}_{12}^0 + \int_{t_0}^{t} \delta\mathbf{a}_{12}(t')dt', \tag{8b}$$

$$\delta\mathbf{a}_{12}(t) = \delta\mathbf{a}_1(t) - \delta\mathbf{a}_2(t). \tag{8c}$$

Note that the range-rate is expressed in terms of the differential accelerations caused by temporal mass variation anomalies exerting on the two satellites, $\delta\mathbf{a}_1(t)$–$\delta\mathbf{a}_2(t)$, and also the incremental initial state difference (or incremental inter-satellite initial state) $\delta\mathbf{r}_{12}^0$ and $\delta\mathbf{v}_{12}^0$. Furthermore, considering the calculated range-rate $\tilde{\dot{\rho}}(t)$, the residual range-rate is defined as $\delta\dot{\rho}(t) = \dot{\rho}(t) - \tilde{\dot{\rho}}(t)$, where $\tilde{\dot{\rho}}(t) = \tilde{\mathbf{v}}_{12}(t)^T\,\tilde{\mathbf{r}}_{12}(t)/\sqrt{\tilde{\mathbf{r}}_{12}(t)^T\tilde{\mathbf{r}}_{12}(t)}$.

[8] Now we express $\delta\mathbf{a}_1(t)$ and $\delta\mathbf{a}_2(t)$ using the parameters associated with the surface mass anomalies. The gravitational acceleration exerted by the i-th surface mass anomaly $\delta m_i(t)$ on the satellite j, can be expressed by approximating the point mass anomaly as follows:

$$\delta\mathbf{a}_{j,i}(t) = \frac{G\delta m_i(t)}{|\mathbf{p}_{j,i}(t)|^2}\frac{\mathbf{p}_{j,i}(t)}{|\mathbf{p}_{j,i}(t)|} = G\frac{(\mathbf{q}_i(t) - \mathbf{r}_j(t))}{|\mathbf{q}_i(t) - \mathbf{r}_j(t)|^3}\delta m_i(t), \tag{9}$$

where G is the gravitational constant and the vectors $\mathbf{p}$, $\mathbf{q}$, and $\mathbf{r}$ are defined as in Figure 1. Note that the surface mass element $\delta m_i(t)$, expressed with a point mass approximation in (9), can be represented in terms of water height equivalent by taking the following expression:

$$\delta m_i(t) = \kappa_w\sigma_i\delta h_i(t), \tag{10}$$

where κ_w is a volumetric density of the water, σ_i is the surface area, and $\delta h_i(t)$ is the water height equivalent distributed uniformly within the area σ_i. The total acceleration being exerted on the satellite is computed by simply adding the contributions from all possible mass anomalies on the surface:

$$\delta\mathbf{a}_j(t) = \sum_{i=1}^{N}\delta\mathbf{a}_{j,i}(t) = G\sum_{i=1}^{N}\mathbf{f}_{j,i}(t)\delta m_i(t), \tag{11}$$

where N is total number of mass anomalies within the region of consideration and $\mathbf{f}_{j,i}(t) = \frac{\mathbf{q}_i(t)-\mathbf{r}_j(t)}{|\mathbf{q}_i(t)-\mathbf{r}_j(t)|^3}$. The acceleration vector difference between the satellites is given by

$$\delta\mathbf{a}_{12}(t) = G\sum_{i=1}^{N}\left(\mathbf{f}_{1,i}(t) - \mathbf{f}_{2,i}(t)\right)\delta m_i(t) = G(\mathbf{F}_1(t) - \mathbf{F}_2(t))\delta\mathbf{m}(t), \tag{12}$$

where $\mathbf{F_1}$ and $\mathbf{F_2}$ are 3-by-N matrices containing the vector elements of $\mathbf{f}_{1,i}(t)$ and $\mathbf{f}_{2,i}(t)$.

[9] We assume $\delta\mathbf{m}(t) = \delta\mathbf{m}$ for a finite interval, i.e., t–t_0, which is roughly some hundred seconds for GRACE satellites passing over the region to cover some tens degrees

in latitude, and compute the integrals associated with inter-satellite state vectors as follows:

$$\int_{t_0}^{t} \delta \mathbf{a}_{12}(t')dt' = G\int_{t_0}^{t} (\mathbf{F}_1(t') - \mathbf{F}_2(t'))dt'\delta\mathbf{m} = \mathbf{H}(t)\delta\mathbf{m}, \quad (13)$$

$$\int_{t_0}^{t}\int_{t_0}^{t'} \delta \mathbf{a}_{12}(t'')dt''dt' = G\int_{t_0}^{t}\int_{t_0}^{t'} (\mathbf{F}_1(t'') - \mathbf{F}_2(t''))dt''dt'\delta\mathbf{m} = \mathbf{S}(t)\delta\mathbf{m}, \quad (14)$$

where the numerical integration following the trapezoidal rule (approximating a straight line) is implemented for computing the matrices $\mathbf{H}(t)$ and $\mathbf{S}(t)$ in this study. Subsequently, we obtain the following expression for the inter-satellite state vectors:

$$\mathbf{r}_{12}(t) = \tilde{\mathbf{r}}_{12}(t) + \delta\mathbf{r}_{12}^0 + \mathbf{S}(t)\delta\mathbf{m}, \quad (15)$$

$$\mathbf{v}_{12}(t) = \tilde{\mathbf{v}}_{12}(t) + \delta\mathbf{v}_{12}^0 + \mathbf{H}(t)\delta\mathbf{m}. \quad (16)$$

Note that the matrices $\mathbf{F_1}$ and $\mathbf{F_2}$ are determined entirely based on the geometric information (i.e., satellite trajectory) of each satellite and point mass anomalies. The nominal position vectors $\tilde{\mathbf{r}}_1$ (t) and $\tilde{\mathbf{r}}_2(t)$ can be used to calculate those matrices without significant model error. Note that we do not adjust the individual (absolute) orbits from the inter-satellite measurements, but adjust the relative orbits.

[10] Since the range-rate observation is a non-linear combination of the position and velocity vectors as defined in (7), we expect the parameters we are interested in such as $\delta\mathbf{m}$ (also $\delta\mathbf{r}_{12}^0$ and $\delta\mathbf{v}_{12}^0$) are non-linearly related with the range-rate through equations (15) and (16). In order to obtain a linearized observation equation, we first consider the inner-product between inter-satellite velocity and position vectors and the norm of inter-satellite position vector and then take their derivatives with respect to the mass anomaly vector and with respect to the incremental initial state vector difference. Those derivatives are explicitly given in Appendix. Using those, we derive the partial derivatives of the range-rate as follows:

$$\frac{\partial\dot{\rho}(t)}{\partial\delta\mathbf{m}} = \left(\mathbf{r}_{12}(t)^T\mathbf{r}_{12}(t)\right)^{-1/2}\frac{\partial\mathbf{v}_{12}(t)^T\mathbf{r}_{12}(t)}{\partial\delta\mathbf{m}} + \left(\mathbf{v}_{12}(t)^T\mathbf{r}_{12}(t)\right)\left(-\frac{1}{2}\right)\left(\mathbf{r}_{12}(t)^T\mathbf{r}_{12}(t)\right)^{-3/2} \cdot \frac{\partial\mathbf{r}_{12}(t)^T\mathbf{r}_{12}(t)}{\partial\delta\mathbf{m}}, \quad (17)$$

$$\frac{\partial\dot{\rho}(t)}{\partial\delta\mathbf{r}_{12}^0} = \left(\mathbf{r}_{12}(t)^T\mathbf{r}_{12}(t)\right)^{-1/2}\frac{\partial\mathbf{v}_{12}(t)^T\mathbf{r}_{12}(t)}{\partial\delta\mathbf{r}_{12}^0} + \left(\mathbf{v}_{12}(t)^T\mathbf{r}_{12}(t)\right)\left(-\frac{1}{2}\right)\left(\mathbf{r}_{12}(t)^T\mathbf{r}_{12}(t)\right)^{-3/2} \cdot \frac{\partial\mathbf{r}_{12}(t)^T\mathbf{r}_{12}(t)}{\partial\delta\mathbf{r}_{12}^0}, \quad (18)$$

$$\frac{\partial\dot{\rho}(t)}{\partial\delta\mathbf{v}_{12}^0} = \left(\mathbf{r}_{12}(t)^T\mathbf{r}_{12}(t)\right)^{-1/2}\frac{\partial\mathbf{v}_{12}(t)^T\mathbf{r}_{12}(t)}{\partial\delta\mathbf{v}_{12}^0} + \left(\mathbf{v}_{12}(t)^T\mathbf{r}_{12}(t)\right)\left(-\frac{1}{2}\right)\left(\mathbf{r}_{12}(t)^T\mathbf{r}_{12}(t)\right)^{-3/2} \cdot \frac{\partial\mathbf{r}_{12}(t)^T\mathbf{r}_{12}(t)}{\partial\delta\mathbf{v}_{12}^0}. \quad (19)$$

Finally the range-rate observation equation (after the first order linearization) can be written as follows:

$$\delta\dot{\rho}(t) = \dot{\rho}\left(t;\delta\mathbf{m},\delta\mathbf{r}_{12}^0,\delta\mathbf{v}_{12}^0\right) - \tilde{\dot{\rho}}(t) \approx \left[\frac{\partial\dot{\rho}(t)}{\partial\delta\mathbf{m}}\ \frac{\partial\dot{\rho}(t)}{\partial\delta\mathbf{r}_{12}^0}\ \frac{\partial\dot{\rho}(t)}{\partial\delta\mathbf{v}_{12}^0}\right]\begin{bmatrix}\delta\mathbf{m}\\ \delta\mathbf{r}_{12}^0\\ \delta\mathbf{v}_{12}^0\end{bmatrix} + e, \quad (20)$$

where e is measurement error associated with the observation $\dot{\rho}(t)$. The range-rate observation is parameterized with the mass anomaly on the surface and with the incremental relative initial state vector. The sensitivity or partial derivative matrix in (20) explicitly consists of two matrices (See also Appendix), $\mathbf{H}(t)$ and $\mathbf{S}(t)$, and the inter-satellite position and velocity vectors, $\mathbf{r}_{12}(t)$ and $\mathbf{v}_{12}(t)$. The absolute position vectors locating each of the orbiting satellites are required for computing $\mathbf{H}(t)$ and $\mathbf{S}(t)$. We fix those absolute position vectors using the a priori calculated orbits on the basis of a reference gravity and force models. On the other hand, the relative orbits sensitive to the range-rate observations are iteratively updated using equation (15) and (16) and used in (17) through (20).

[11] The number of point mass anomalies depends on how one chooses the size of area and grid, however one will have 6 additional parameters (incremental relative initial state vector) per each overpass (short arc over the region) no matter how many the regional mass anomalies are. The latter arc-dependent parameters are necessary primarily due to temporal mass anomalies outside of the focus region and also caused by un-modeled and mis-modeled a priori forces (including the accelerometer measurement error). As we will see in the later section, these arc-dependent parameters are useful to reduce long wavelength error and signal in the range-rate data not associated with the temporal mass variation over the local area. The surface mass variations are the parameters common to all short arcs while each incremental initial state parameter is sensitive only to the data in individual short arc. For example, if we have N mass points, M short arcs over the region of interest, and L samples per each arc, we have $L \times M$ observations and $N + 6M$ parameters. With M greater than N, the redundancy asymptotically approaches the constant $L/6$ that depends only on the number of range-rate observations in each overpass.

2.2. Representation of Mass Anomaly on the Surface

[12] In the previous section, we have developed the range-rate observation equation by approximating the surface mass anomaly as point mass when formulating the gravitational acceleration in equation (9). The error in this approximation certainly will depend on the size of the surface area σ_i introduced in equation (10). Ideally we want

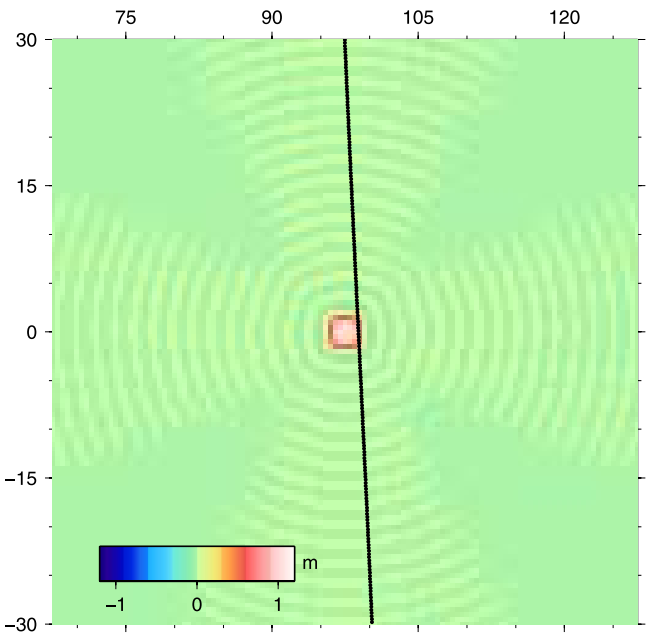

Figure 2. The mass anomaly on the Earth's surface in terms of water height equivalent is depicted. 1 m of water mass is distributed uniformly in a 3° × 3° block area. The plot shows the water height represented by spherical harmonic expansion with the maximum degree of 180. An actual GRACE ascending track (450 km in altitude) nearby the mass anomaly is also shown.

to have a representation for the acceleration vector caused by mass anomaly in a block on the Earth's surface. The expression of the gravitational attraction caused by a finite-size surface mass anomaly can be done by expanding it on the basis of the spherical harmonic series. However, if we truncate the spherical harmonic series for practical purpose, it will essentially result in just another (global) approximation of the (local) surface mass block with spherical harmonics. In this section we will quantify the truncation error of the spherical harmonic series and the error introduced by using a point mass formulas, equations (9) and (10), for computation of the acceleration vector.

[13] The following shows how we derive the spherical harmonic expression of the finite size mass anomaly on the Earth surface. First, we consider an infinitesimal mass anomaly dm on the Earth's surface exerting gravitational potential dV on a distant location above the Earth's surface as follow:

$$dV(r,\theta,\lambda) = G\frac{dm(r',\theta',\lambda')}{l(r,\theta,\lambda,r',r',\theta',\lambda')} \tag{21}$$

$$\frac{1}{l(r,\theta,\lambda,r',\theta',\lambda')} = \sum_{n=0}^{\infty}\sum_{m=0}^{n}\frac{1}{2n+1}\left[\frac{\bar{R}_{nm}(\theta,\lambda)}{r^{n+1}}r'^{n}\bar{R}_{nm}(\theta',\lambda') + \frac{\bar{S}_{nm}(\theta,\lambda)}{r^{n+1}}r'^{n}\bar{S}_{nm}(\theta',\lambda')\right], \tag{22}$$

where l is the linear distance between the two points, (r, θ, λ) and (r', θ', λ'), i.e., the location of satellite and surface mass, in spherical coordinates (radius, co-latitude, longitude). Equation (22) can be derived by using the decomposition formula as shown by *Heiskanen and Moritz* [1967]. $\bar{R}_{nm}$ and $\bar{S}_{nm}$ are the 4π-normalized surface harmonic functions, i.e., multiplication of the normalized associated Legendre function and either cosine or since functions, respectively. If the mass anomaly $dm(r', \theta', \lambda')$ is distributed homogeneously only within a finite area of $\theta_1 \le \theta' \le \theta_2$ and $\lambda_1' \le \lambda' \le \lambda_2'$ on the surface of the spherical Earth with the radius r', we can get the following expression:

$$dV(r,\theta,\lambda) = G\rho_w h r'^2 \int_{\lambda_1}^{\lambda_2}\int_{\theta_1}^{\theta_2}\frac{\sin\theta' d\theta' d\lambda'}{l(r,\theta,\lambda,r',\theta',\lambda')}, \tag{23}$$

since $dm(r', \theta', \lambda') = \rho_w h r'^2 \sin\theta' d\theta' d\lambda'$ with the volumetric density of the water ρ_w and the water height h resulting the surface density $\rho_w h$. Putting (22) into (23), we get

$$dV(r,\theta,\lambda) = G\rho_w h r'^2 \sum_{n=0}^{\infty}\sum_{m=0}^{n}\frac{1}{2n+1} \cdot \left[\frac{\bar{R}_{nm}(\theta,\lambda)}{r^{n+1}}r'^{n}\int_{\lambda_1}^{\lambda_2}\int_{\theta_1}^{\theta_2}\bar{R}_{nm}(\theta',\lambda')\sin\theta' d\theta' d\lambda' + \frac{\bar{S}_{nm}(\theta,\lambda)}{r^{n+1}}r'^{n}\int_{\lambda_1}^{\lambda_2}\int_{\theta_1}^{\theta_2}\bar{S}_{nm}(\theta'\lambda')\sin\theta' d\theta' d\lambda'\right] \tag{24}$$

Accounting for the elastic loading effect of the solid Earth and adding together the contribution of all the grid cells, we obtain

$$\delta V(r,\theta,\lambda) = G\rho_w r' \sum_{n=0}^{\infty}\sum_{m=0}^{n}\left(\frac{r'}{r}\right)^{n+1}\left[\left\{\sum_{i=1}^{I}\frac{(1+k_n)\delta h_i}{2n+1}\int_{\lambda_i}^{\lambda_i+\Delta\lambda}\int_{\theta_i}^{\theta_i+\Delta\theta}\bar{R}_{nm}(\theta',\lambda')\sin\theta' d\theta' d\lambda'\right\}\bar{R}_{nm}(\theta,\lambda) + \left\{\sum_{i=1}^{I}\frac{(1+k_n)\delta h_i}{2n+1}\int_{\lambda_i}^{\lambda_i+\Delta\lambda}\int_{\theta_i}^{\theta_i+\Delta\theta}\bar{S}_{nm}(\theta',\lambda')\sin\theta' d\theta' d\lambda'\right\}\bar{S}_{nm}(\theta,\lambda)\right], \tag{25}$$

where k_n is the load Love number [*Han and Wahr*, 1995]. We now compare (25) with the following expression:

$$\delta V(r,\theta,\lambda) = \frac{GM}{r'}\sum_{n=0}^{\infty}\sum_{m=0}^{n}\left(\frac{r'}{r}\right)^{n+1} \cdot [\delta\bar{A}_{nm}\bar{R}_{nm}(\theta,\lambda) + \delta\bar{B}_{nm}\bar{S}_{nm}(\theta,\lambda)], \quad (26)$$

where M is the mean mass of the Earth. Therefore we obtain the spherical harmonic coefficient of the gravitational potential in terms of water height equivalent, δh_i, distributed uniformly within each block defined by $\theta_i \le \theta' \le \theta_i + \Delta\theta$ and $\lambda_i \le \lambda' \le \lambda_i + \Delta\lambda_i$ as follows:

$$\delta\bar{A}_{nm} = \frac{(1+k_n)(r')^2\rho_w}{(2n+1)M} \cdot \sum_{i=1}^{I}\left\{\int_{\lambda_i}^{\lambda_i+\Delta\lambda}\int_{\theta_i}^{\theta_i+\Delta\theta}\bar{R}_{nm}(\theta',\lambda')\sin\theta' d\theta' d\lambda'\right\}\delta h_i, \quad (27)$$

$$\delta\bar{B}_{nm} = \frac{(1+k_n)(r')^2\rho_w}{(2n+1)M} \cdot \sum_{i=1}^{I}\left\{\int_{\lambda_i}^{\lambda_i+\Delta\lambda}\int_{\theta_i}^{\theta_i+\Delta\theta}\bar{S}_{nm}(\theta',\lambda')\sin\theta' d\theta' d\lambda'\right\}\delta h_i, \quad (28)$$

where $\int_{\lambda_i}^{\lambda_i+\Delta\lambda}\int_{\theta_i}^{\theta_i+\Delta\theta}\bar{R}_{nm}(\theta',\lambda')\sin\theta' d\theta' d\lambda' = \int_{\theta_i}^{\theta_i+\Delta\theta}\bar{P}_{nm}(\theta')\sin\theta' d\theta' \int_{\lambda_i}^{\lambda_i+\Delta\lambda}\cos(m\lambda')d\lambda'$, $\int_{\lambda_i}^{\lambda_i+\Delta\lambda}\int_{\theta_i}^{\theta_i+\Delta\theta}\bar{S}_{nm}(\theta',\lambda')\sin\theta' d\theta' d\lambda' = \int_{\theta_i}^{\theta_i+\Delta\theta}\bar{P}_{nm}(\theta')\sin\theta' d\theta' \int_{\lambda_i}^{\lambda_i+\Delta\lambda}\sin(m\lambda')d\lambda'$, and $\bar{P}_{nm}(\theta')$ is the associated Legendre function. While the integration of the sine and cosine functions is trivial, the integration of the normalized associated Legendre function can be computed recursively following the algorithm given by *Paul* [1978], for example. Equations (27) and (28) indicate that each spherical harmonic coefficient can be calculated by summing each of the mass anomalies distributed on the surface. They are also derived by several other authors in various ways (for example, *Chao et al.* [1987]).

[14] Finally, the gravitational acceleration vector exerting on the satellites in the Earth-centered and fixed (ECF) frame can be derived by taking derivatives of (26) with (27) and (28) in radial, north (co-latitude) and east (longitude) directions and by rotating the vector in the local north-east-down triad to the ECF frame. Later, the numerical integration will be done in the inertial frame after rotating the acceleration vector in the ECF frame to the inertial frame. Consequently, we can derive the *linear* relationship between the acceleration vector in the inertial frame and the equivalent water height on the Earth surface in the same way as a point mass representation but via spherical harmonic expression. Note that, in both cases, the acceleration vector is parameterized in terms of the water height equivalent, which is a constant in each block. The only error associated with the spherical harmonic representation is the truncation of the harmonic series.

[15] Now we numerically calculate the truncation error that is dependent on the maximum degree of expansion and the approximation error that is committed by assuming that all the mass within the block is concentrated on a center point. For the time-variable gravity from the GRACE satellite tracking data, we typically consider a block of a few hundred km in each direction. We test how the surface mass anomaly uniformly distributed within a block of 330^2 km^2 (or $3° \times 3°$ at the equator) perturbs the satellite-to-satellite range-rate when the satellites overpass the mass block. Figure 2 shows 1 m of water mass equally distributed in a $3° \times 3°$ block centered at 0°N and 97.5°E and an actual ascending GRACE ground track. In the Figure, the mass anomaly has been calculated by using spherical harmonic expansion up to degree and order 180. There are tiny but global oscillations outside the block due to truncation. We integrated the gravitational acceleration vector exerted on the satellites to calculate the relative orbits and the range-rate perturbation along the nominal orbits using the approach shown in the previous section (See equations (7) and (8)). We also forced the incremental inter-satellite initial state to be zero at the South pole for the ascending orbit. To calculate the acceleration vector, we used three approaches including the spherical harmonic expansion of the surface mass anomaly truncated to the maximum degree of 180 and 60 and the point mass formulation. Figure 3 presents range-rate perturbation along the ascending orbit. We initiated numerical integration of the acceleration vectors from the South pole by fixing the initial state (position and velocity vector) with the nominal state that yields zero range-rate perturbation at the starting point. The dot-dashed line indicates the perturbation calculated on the basis of spherical harmonic expansion up to degree and order 180. The dashed line is its deviation from the one calculated by point mass formula given in equations (9) and (10) and the solid line shows the difference caused by truncating the maximum degree to 60 as opposed to 180. Assuming the spherical harmonic expansion up to degree and order 180 represents the actual mass anomaly within the block with negligible truncation error (beyond 180), we identify the maximum error committed by assuming the mass is concentrated on a central point is an order of magnitude smaller (±0.03 μm/s) than the currently operating GRACE range-rate error (0.2–0.3 μm/s in RMS sense). In this simulation, we assumed a very large amount of mass such as 1 m of water height equivalent implying the dashed line would be the bound of the algorithmic error we make by using the point mass formulation. The maximum error committed by truncating the spherical harmonic series to degree 60 is confined within ±0.01 μm/s. Certainly both the truncation error and point mass approximation error will depend on the size of the block we consider. The smaller the size of the block, the larger the truncation error (if we fix the maximum expansion degree) but the smaller the point mass approximation error, since the smaller size is getting closer to a point mass. If we consider a future mission like GRACE follow-on, we should reduce the size of the block, however, for the current GRACE data processing, we use $\sim 330^2$ km^2 equal area block and a point mass attraction for computing acceleration since it drastically reduces the computational time.

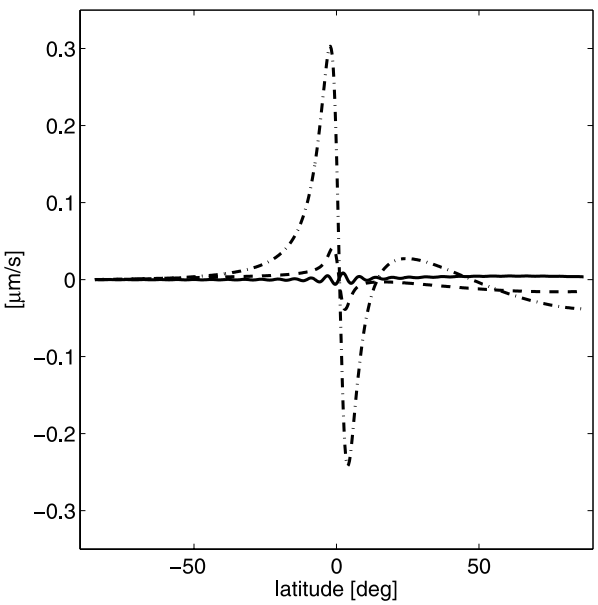

Figure 3. Perturbation in range-rate caused by the mass anomaly depicted in Figure 2 is calculated along the actual GRACE orbit by numerically integrating the acceleration vector formed by the spherical harmonic series with maximum degree 180 (dot-dashed). The range-rate perturbation is also calculated by integrating the acceleration vector computed by a point mass approximation and it gives the maximum deviation from the 180 spherical harmonic expression within ±0.03 μm/s (dashed). The truncation to the maximum degree of 60 yields the deviation within ±0.01 μm/s (solid).

2.3. Parameterization of Temporal Variability

[16] Previously, we established a linear relationship between the gravitational acceleration exerted between the satellites and the mass anomaly (or water height equivalent) on the surface by a point mass formula and by spherical harmonic representation of a block mean mass. Further, we developed a non-linear observation equation between the instantaneous inter-satellite tracking data and the *mean* mass variation expressed in terms of water height equivalent. Here we refine the observation equation by parameterizing the temporal variation of the mass anomaly in each block. A typical duration of each short overpass arc is 600 s if our focus region covers 40° in latitude because the along-track speed of the orbiting GRACE satellites is about 7–8 km/s. Within this period (duration of each overpass arc) we can reasonably assume constant mass anomaly, i.e., $\delta\mathbf{m}(t) = \delta\mathbf{m}$ (or $\delta\mathbf{h}(t) = \delta\mathbf{h}$). However, for the tracking data along the next overpass after one revolution (1.5 h later), the mass anomaly in the region may no longer be the same constant as before, especially around the area under the influence of large (remaining) ocean tides. We may use many days of tracking data to solve for the time-averaged mass variation disregarding any temporal variability within the period and its aliasing effect to the mean mass estimates. On the other hand, we can extend the observation equation by parameterizing the mass variation with some analytic functions. For example, we parameterize the surface mass anomalies as follows:

$$\delta h_i(t) = C_i^0 + S_i^0(t - t_0) + C_i^1 \cos(\omega_1 t) + S_i^1 \cos(\omega_1 t) + \ldots, \tag{29}$$

where $\delta h_i(t)$ is mass variation (in terms of water height) at the i-th location at time t. C_i^0 and S_i^0 are offset and coefficient of a linear trend at i-th location. C_i^1 and S_i^1 are coefficients of the first frequency (for example, annual frequency or tidal frequency) at i-th location and so on. The parameters to be determined from the data are the respective coefficients of each analytic function at every location, i.e., C_i^0, S_i^0, C_i^1, S_i^1, etc. The harmonic (temporal) frequency components to be included depend on the geographical location and the application. For example, on land, the annual and semi-annual variations would be included for estimating seasonal terrestrial water storage change. On coastal region and polar Seas including the ice shelves, where the a priori ocean tide model is not performing well, the tidal frequencies (roughly once or twice per day) can be included in addition to seasonal frequencies. Instead of solving the mass variation with a fixed interval, the respective coefficients of the modeled functions are estimated. Of course the solution would depend on how we model the temporal variability in the region. The temporal parameterization is established simply by applying the following linear equation to the observation equation, equation (20):

$$\begin{bmatrix} \delta h_1 \\ \delta h_2 \\ \vdots \\ \delta h_I \end{bmatrix} = \begin{bmatrix} \mathbf{t}_1^T \delta\mathbf{c}_1 \\ \mathbf{t}_2^T \delta\mathbf{c}_2 \\ \vdots \\ \mathbf{t}_I^T \delta\mathbf{c}_I \end{bmatrix} = \mathbf{T}\delta\mathbf{c}, \tag{30}$$

where a vector $\mathbf{t}_i$ contains the modeled temporal functions and $\delta\mathbf{c}_i$ is the respective coefficients at i-th location. The way to model temporal variations (how many and which harmonic frequencies to be used) can be varied at every block. It is not necessary to apply the same temporal functions uniformly at each location. If we assume L elements used to describe the temporal variation at each location and there are I grid points in the region, the matrix $\mathbf{T}$ contains I rows and $L \times I$ columns and the number of total unknown parameters (size of the vector $\delta\mathbf{c}$) to be solved for is $L \times I$. This approach is particularly useful to estimate the mass variation with known temporal behaviors such as tides with given frequencies.

2.4. Solid Earth Loading

[17] If we use the point mass formula, the estimates are not the actual water mass anomaly but the one influenced by elastic deformation caused by its loading on the solid Earth. Without considering the loading effect, we underestimate the actual mass. To obtain the actual mass anomaly from the estimated mass parameter δh_i (apparent water mass) after the least squares inversion of range-rate observations, we

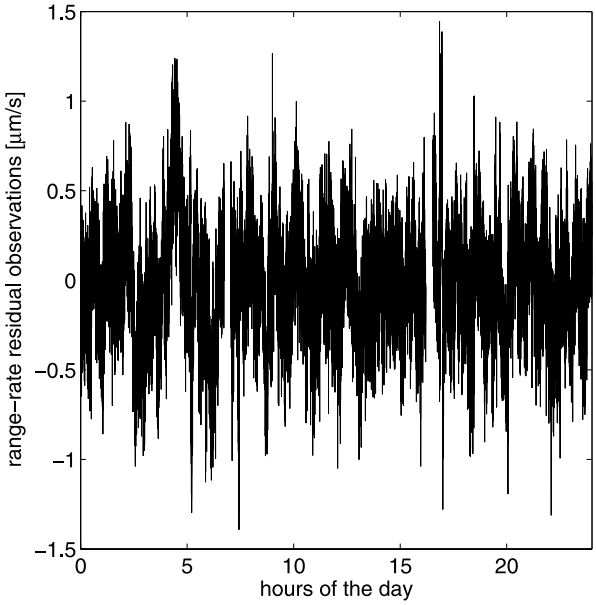

Figure 4. Difference of the range-rates determined from the calculated state (position and velocity) vectors of the two satellites and observed from the onboard satellite-to-satellite tracking instrument. Note that the range-rate residual data depicted here contain the effects caused mostly by temporal variability of the gravity fields. There are two phase-unlocks during this particular day as indicated by two gaps in the time series.

compute the spherical harmonic spectra as follows (the same as (27) and (28) except the factor $1 + k_n$):

$$\delta\bar{A}_{nm} = \frac{(r')^2\rho_w}{(2n+1)M}\sum_{i=1}^{I}\left\{\int_{\lambda_i}^{\lambda_i+\Delta\lambda}\int_{\theta_i}^{\theta_i+\Delta\theta}\bar{R}_{nm}(\theta',\lambda')\sin\theta' d\theta' d\lambda'\right\}\delta h_i, \tag{31}$$

$$\delta\bar{B}_{nm} = \frac{(r')^2\rho_w}{(2n+1)M}\sum_{i=1}^{I}\left\{\int_{\lambda_i}^{\lambda_i+\Delta\lambda}\int_{\theta_i}^{\theta_i+\Delta\theta}\bar{S}_{nm}(\theta',\lambda')\sin\theta' d\theta' d\lambda'\right\}\delta h_i, \tag{32}$$

Then we evaluate the coefficients to obtain the actual water mass only within the region we considered by taking into account for the load Love number, k_n as follows [also *Wahr et al.*, 1998]:

$$\delta h(\theta,\lambda) = \frac{R\rho_E}{3\rho_w}\sum_{n=0}^{N_{\max}}\frac{2n+1}{1+k_n}\sum_{m=0}^{n}[\delta\bar{A}_{nm}\bar{R}_{nm}(\theta,\lambda) + \delta\bar{B}_{nm}\bar{S}_{nm}(\theta,\lambda)], \tag{33}$$

where R is a mean radius of the Earth and ρ_E and ρ_w are the mean density of the Earth and water. Note the equation (33) is valid for evaluation within the region we used for the estimation because we calculated localized spherical harmonic coefficients through (31) and (32) only using the regional signals. The loading effect caused by the (disregarded) neighboring surface mass is generally as small as a few mm in water height equivalent.

3. Result and Analysis

[18] We first describe how we determine the nominal satellite trajectory. The a priori orbits are later used to register and reduce range-rate observations by removing the major signals caused by the mean gravity field and some of better-known mass variations such as planetary perturbation, tides, and atmosphere. We discuss the distinct contributions of regional mass variation and incremental inter-satellite initial state to the range-rate observations. The estimated mass variations over the various regions are presented and compared with the monthly global analysis results in the aspects of spatial and temporal resolutions. At last, the ocean tidal signal recovery after applying (temporal) harmonic functions of some tidal frequencies is discussed.

[19] Fundamental to the extraction of gravity signal from the GRACE inter-satellite range-rate observations is the highly accurate knowledge of the satellite positions, velocities, orientations and calibrated accelerometer observations to account for non-gravitational forces. Following the methodology detailed by *Luthcke et al.* [2006], a simultaneous reduction of the GRACE KBRR and precise orbit ephemeris data is performed in 24-h arcs estimating accelerometer calibration parameters along with GRACE A and B initial state vectors (see *Luthcke et al.* [2006] for arc parameter details). The Goddard Space Flight Center's GEODYN precision orbit determination and geodetic parameter estimation software [*Pavlis et al.*, 2006] is used to reduce these data within the daily arcs using iterative weight least squares estimation. The non-gravitational forces are accounted for by applying the level 1B accelerometer observations along with the estimation of the accelerometer calibration parameters as noted above. The orientation of the GRACE satellites is modeled using the GRACE level 1B quaternion data. The force modeling includes the GGM02C GRACE gravity model through degree and order 120 [*Tapley et al.*, 2004b]. The ocean tides are modeled according to GOT00 [*Ray*, 1999; *Ray and Ponte*, 2003], where M_2 is modeled to degree and order 70, and other major constituents are modeled to degree and order 50. The atmospheric gravity is forward-modeled following *Chao and Au* [1991] using potential coefficients to degree and order 50 at six-hour intervals derived from NCEP pressure grids [*Petrov and Boy*, 2004] assuming inverted barometer effect for the ocean response. The Earth tides are modeled according to the IERS Standards [*IERS*, 2003].

[20] The calculated range-rate from the precise orbit, consequently, reflects the GGM02C gravity model and the aforementioned force models (GOT00 for ocean tide, for example). Its deviation from the measured range-rate, i.e., range-rate residual (RRR), infers the deviation of the instantaneous gravity field with respect to the applied models and is caused mostly by time-variable mass redistribution on the Earth's surface. Figure 4 shows the RRR data on a particular day. We can see the range-rates calculated from the relative velocity and position vectors are in the agreement within ±1.5 μm/s with the KBRR measurement (as accurate as 0.2 μm/s) and those deviations

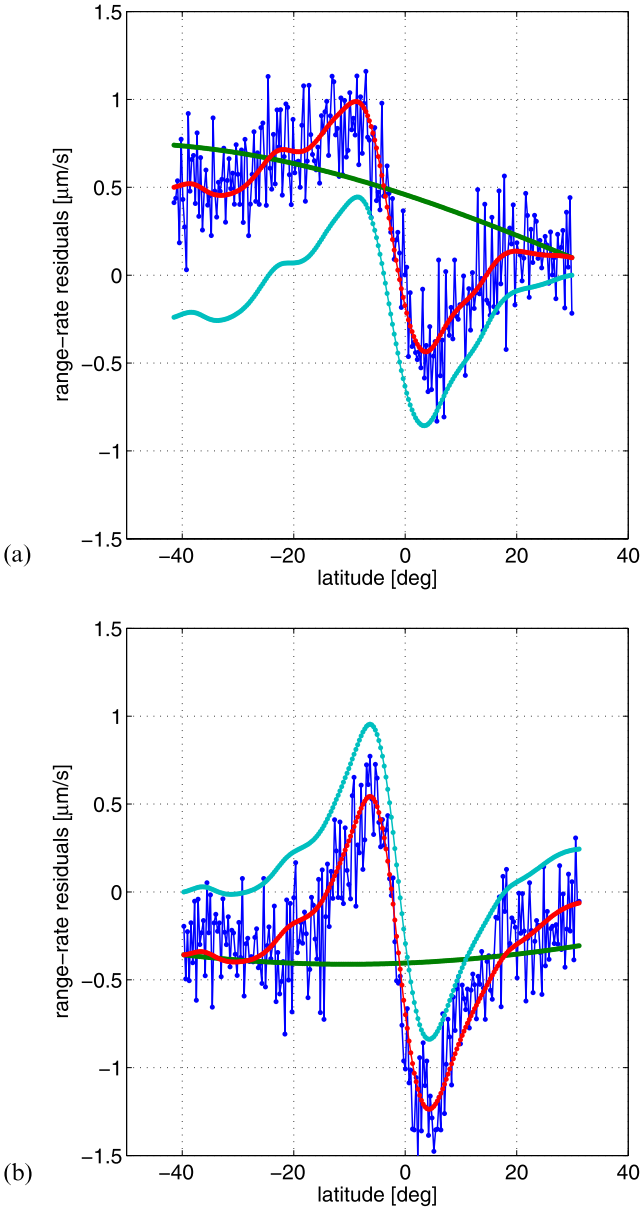

Figure 5. K-Band range-rate residual (RRR) data (Blue) across South America; (a) descending track crossing at the longitude of 305°E–308°E and (b) ascending track crossing at the longitude of 297°E–300°E. After the least squares adjustment of the mass anomaly on the surface and incremental relative initial state vectors, the fit to RRR measurement from the estimates is shown as the red curves. Each contribution from the mass anomaly and initial state parameters is depicted as cyan and green, respectively (consequently, red = cyan + green). The post-fit residual, difference between the fits (red) and measurements (blue), is 0.23 μm/s in RMS. The ground track of (a) is also depicted in Figure 6 to highlight the long-term trend (mostly linear) in RRR not associated with the mass anomaly in the region.

include the effect of instantaneous gravitational perturbation with respect the applied background models.

[21] Figure 5 shows the RRR observations when the two GRACE satellites pass through South America including the Amazon basin along the descending (a) and ascending tracks (b). The descending and ascending tracks overpass at the longitudes of 305°E–308°E and 297°E–300°E, respectively. The RRR data show a pulse-like anomaly as well as high-frequency noise. In addition, we observe long-term trends in RRR of each overpass arc, which is mostly a linear in descending arc and a negative bias in ascending arc. Using 15-days of those RRR data over the region, we estimated the mass anomalies on the surface and the incremental inter-satellite initial state in every arc. The parameters reflecting the mass anomalies are common for all short arc RRR data and they are fixed as constant within the 15-day period allowing estimation of the 15-day averaged mass variation. The incremental inter-satellite initial state parameters independently modeled in each arc reflect the effect of un-modeled and mis-modeled forces (including errors in non-gravitational force modeling and accelerometer measurements) in the calculation of a priori orbits and the mass anomalies outside the region of interest. The initial epoch could be either at the northern or southern boundary of the region for descending or ascending arc, respectively. For the least squares estimation, we adopt a priori spatial constraints for the mass anomaly on the surface as shown by *Rowlands et al.* [2005] and *Han et al.* [2005b] and a priori variances for the initial relative state vectors. We do not rule out various other ways to obtain smoothed or regularized solutions, for example, as described by *Koch and Kusche* [2002].

[22] After the least squares adjustment, we obtained two sets of parameters, i.e., mass distribution (common estimates) and incremental inter-satellite initial state (arc-dependent estimates) in every overpass. We have calculated the RRR effects caused by the mass parameter and initial state parameter separately. In Figure 5, the range-rate perturbations predicted by the mass variation, by the initial state, and by both parameters are presented. The systematic pattern in the observed RRR is interpreted by two distinct components. For the descending arc in Figure 5a, the gradually increasing (from the north), long wavelength feature is suspected to originate not from the mass anomalies in the confined region but possibly from errors in the a priori orbits, accelerometer, and other forces. Note that deviation in the range-rate (difference of measured range-rate and calculated one), i.e., error in the a priori orbit at the initial epoch may cause long-term trend when integrated over time. On the other hand, the pulse-like pattern in the observed RRR is likely to be caused by mass variation in the region. For the ascending arc in Figure 5b, there is a bias in the observed RRR not originating from the mass anomaly in the confined region while the same mass variation (as in the descending overpass) causes the similar pulse-like pattern in the RRR data.

[23] Figure 6 shows the same as Figure 5 but includes all RRR data for 15-days period presenting RRR observations (a), calculated RRR from the mass anomaly estimates (b), and calculated RRR from the incremental inter-satellite initial state estimates (c). In the observations, there are several profiles including long-term trend such as the one pointed with the arrow symbol which is also depicted in Figure 5a. This feature indicating unusually large arc-dependent long-term pattern is not common in other observations. The RRR caused by the mass estimates shown in (b) indicates large perturbation mostly gathered only within

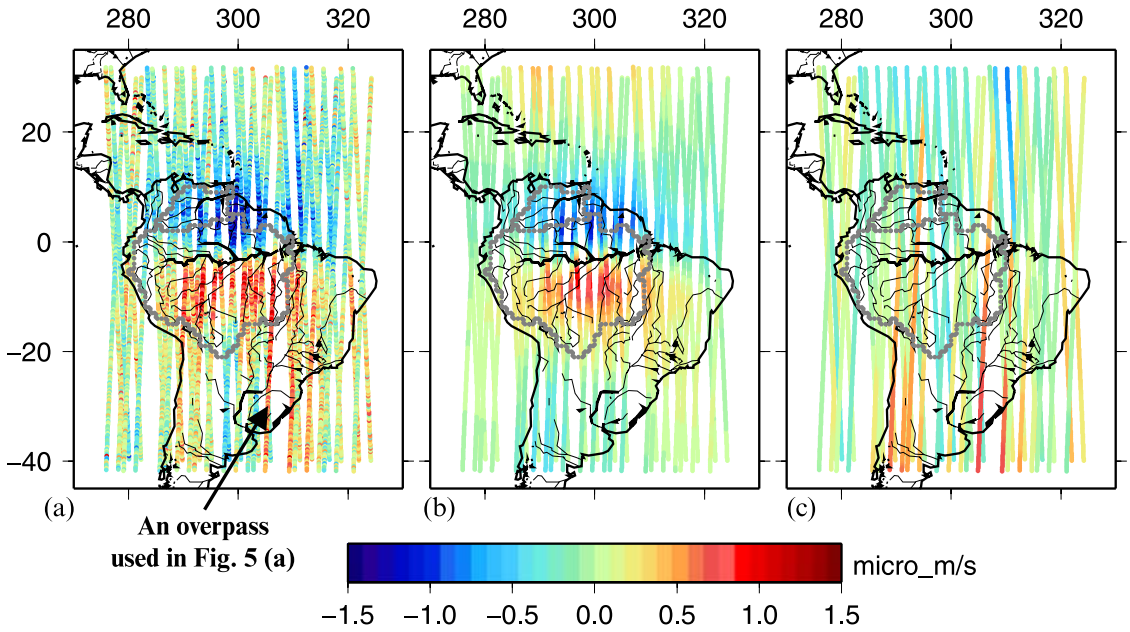

Figure 6. (a) Range-rate residual observations for 15-days period; (b) the fit calculated only using the mass anomaly estimates; (c) the fit predicted only from the incremental relative initial state estimates. Note that most of large perturbation in RRR is focused within the Amazon and Orinoco river basins. A few RRR data contain uncommon and suspicious long-term along-track variations, likely not associated with the mass variation within the region. The effects of the mass anomaly (common parameter) and initial state (arc-dependent parameter) to the range-rate are quite distinct as shown in Figures 6b and 6c, respectively.

the Amazon basin. The RRR caused by initial state estimates shown in (c) looks mostly N-S pattern and there seems to be no correlation between two arcs. The observation noise after taking out (b) and (c) from (a) is quite random yielding 0.23 μm/s of variability in a RMS sense. The RRR observations include the effects of mass variation confined within a certain region, arc-dependent signal or error not associated with the mass variation in the region, and random noise. Figure 7 shows the same as Figure 6 but 6 months later. The sign of the observations has changed with respect to the equator due to the seasonal climate change. Most of large variation is confined within the

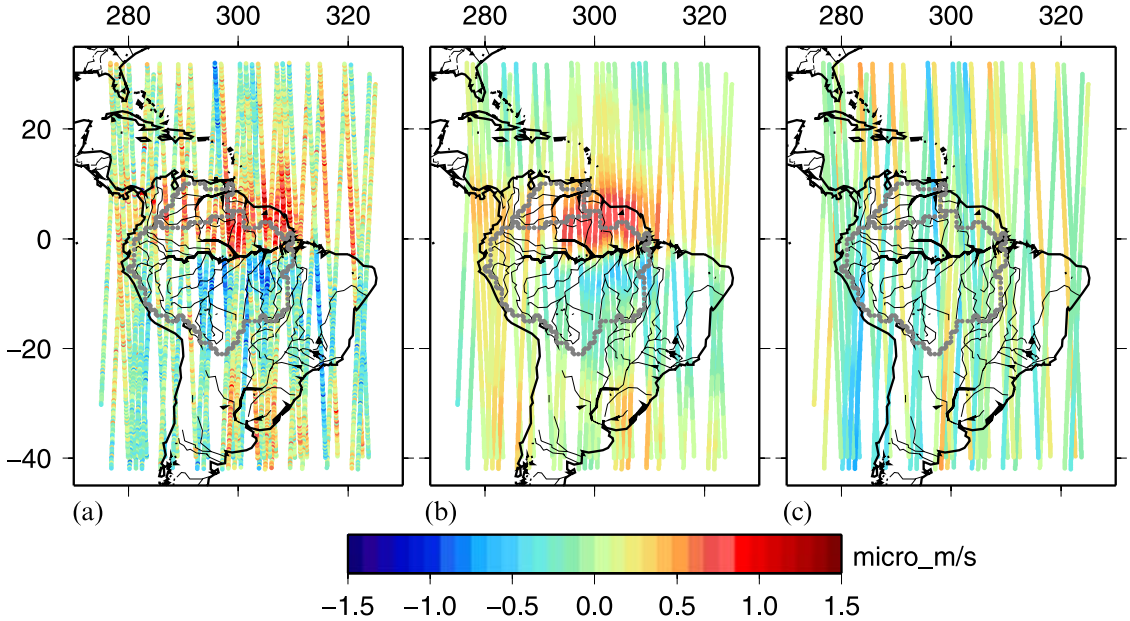

Figure 7. The same as Figure 6, but 6 months later. The opposite variation (compared to Figure 6) after a half year indicates the seasonal variation of terrestrial water in the region.

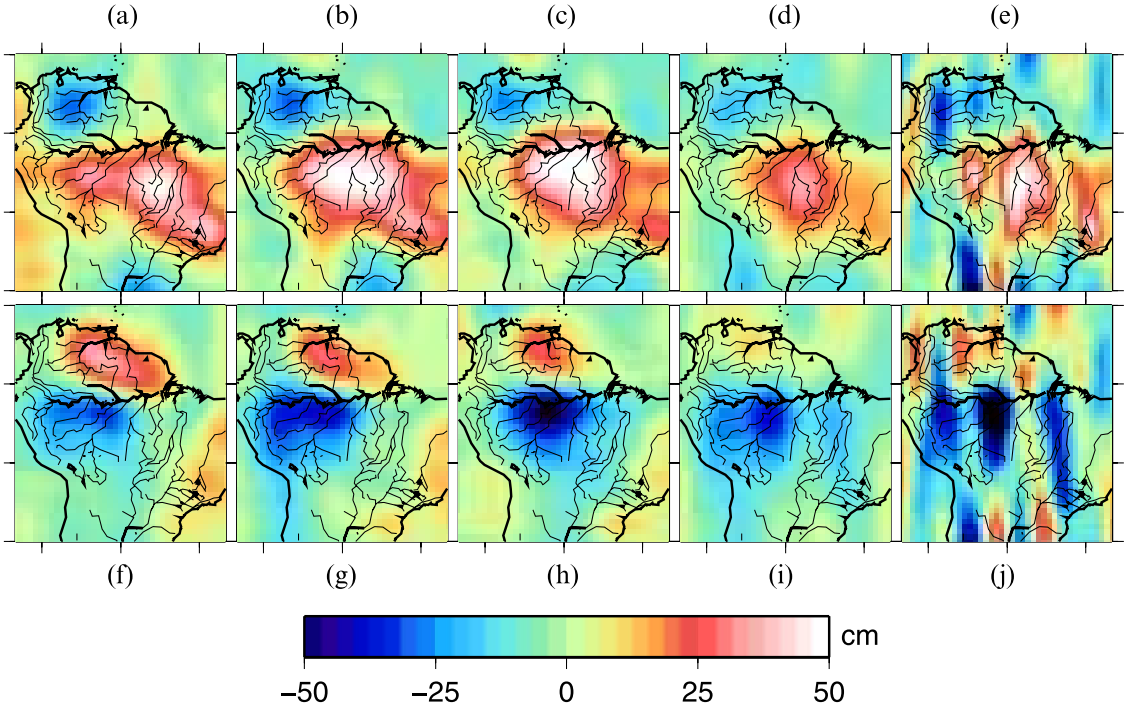

Figure 8. Water storage variation in South America estimated from the localized analysis of RRR data every 15-day interval; first half of March (a), second half of March (b), and first half of April (c) in year 2005. The estimates from the monthly mean global harmonic solutions in March of 2005, (d) and (e), after the Gaussian smoothing with 500 km and 300 km averaging radius, respectively. (f) through (j) are the same as (a) through (e) but 6 month later.

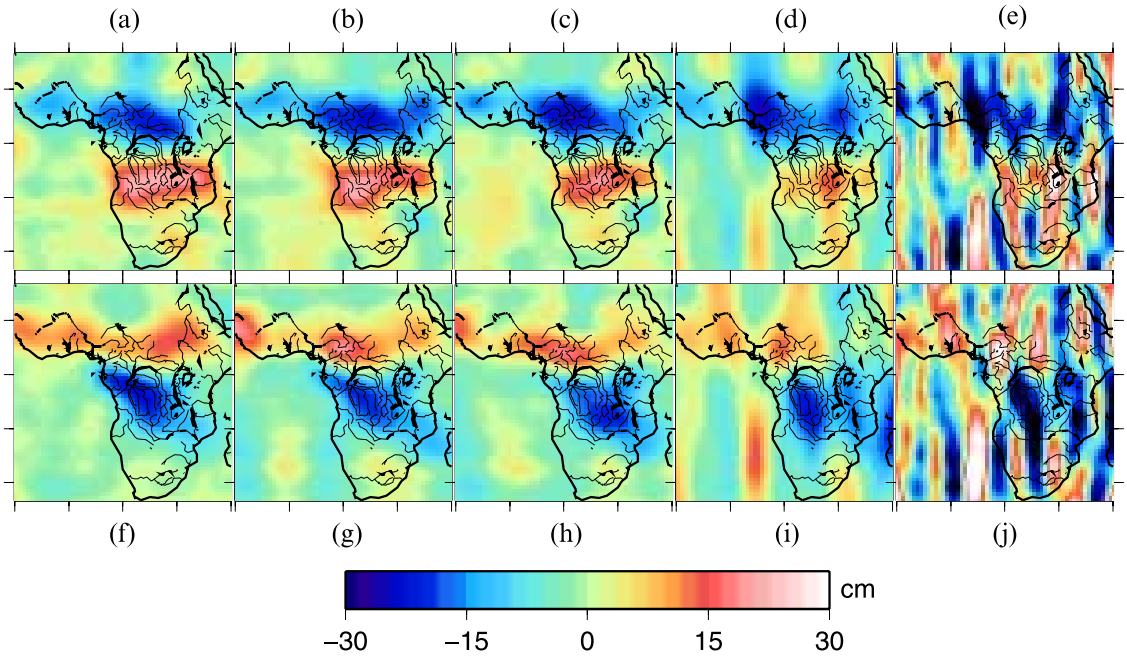

Figure 9. Water storage variation in Africa estimated from the localized analysis of RRR data every 15-day interval; second half of March (a), first half of April (b), and second half of April (c) in year 2005. The estimates from the monthly mean global harmonic solutions in April of 2005, (d) and (e), after the Gaussian smoothing with 500 km and 300 km averaging radius, respectively. (f) through (j) are the same as (a) through (e) but 6 month later.

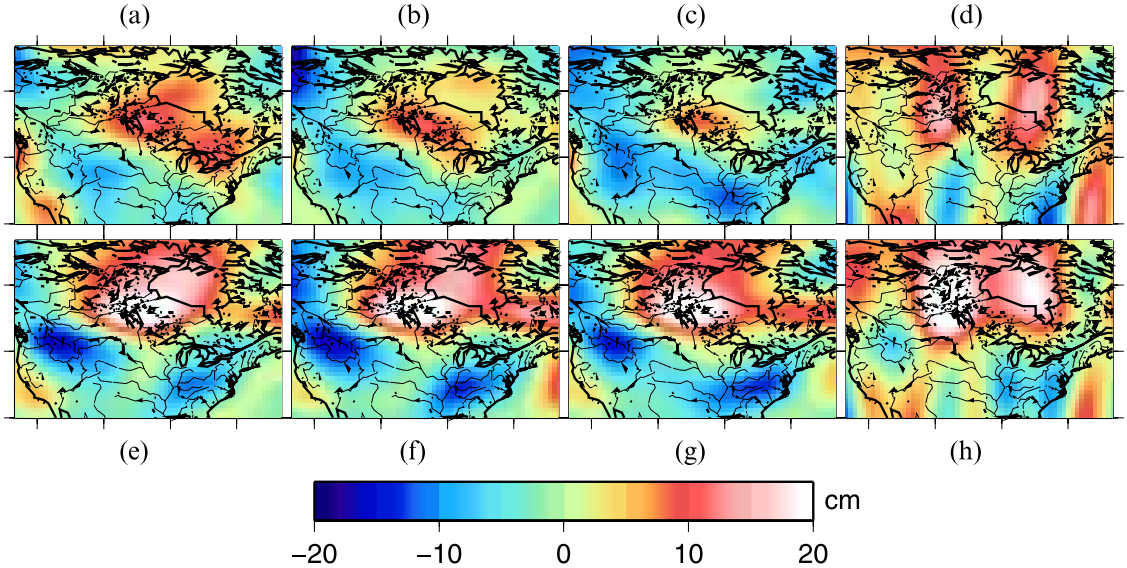

Figure 10. Water storage variation in North America estimated from the localized analysis of RRR data every 15-day interval; first half of September (a), second half of September (b), and first half of October (c) in year 2004. The estimates from the monthly mean global harmonic solutions in September of 2004 (d) after the Gaussian smoothing with 500 km averaging radius. (e) through (h) are the same as (a) through (d) but one year later. Large inter-seasonal variation can be seen.

Amazon basin for both seasons. We also see that the RRR data include mostly temporal variations with little information about the update of the mean gravity field from the comparison of Figures 6 and 7. This is expected because we used the improved mean gravity field model GGM02C as opposed to GGM01C [*Tapley et al.*, 2005].

[24] We have processed 3.5 years of GRACE RRR data for estimating the 15-day mass variation in South America including Amazon basin, Africa including Congo basin, and North America including Mississippi basin and Hudson Bay. Figures 8(a)-(c) show gradual migration of the water storage estimates during the high water season including the first half of March (a), the second half of March (b), and the first half of April in 2005 (c) from the localized analysis of the GRACE data. We can see water storage is being developed from the southeast toward the central Amazon. On the other hand, (d) and (e) are the monthly mean water storage on the month of March in 2005, calculated from the global spherical harmonic series inferring the monthly mean geopotential anomaly, after applying the Gaussian smoothing with averaging radius of 500 km and 300 km, respectively. We have used the latest release of the monthly global gravity solution like CSR RL04 available from the Web site (http://podaac.jpl.nasa.gov/grace/). The global (spatial) smoothing approach may reduce much of signals with too aggressive smoothing (500 km) or yields undesired errors with too conservative smoothing (300 km). The localized analysis, however, retrieved stronger signal without much of error. We also checked the low water season from the localized analysis; (f) through (h) (the second half of August, the first half of September, and the second half of September in 2005). It is clear to identify gradual disappearance of the positive water storage in the north of Amazon River and gradual development of negative anomalies along the Amazon mainstream. The Amazon particularly suffered extreme dry situation in 2005 as also seen from our GRACE analysis by comparing the anomaly in 2005 low water season with the ones in other years (not depicted here). Figures 8i and 8j are from the monthly mean global analysis with smoothing radius of 500 km and 300 km, respectively. Again, the result from global approach with spatial smoothing is either too smooth or too noisy compared to the localized analysis, implying ineffective modeling of the regional anomaly with global basis function like spherical harmonics. The monthly global solutions from the different analysis center like GFZ (not shown here), which are also available from the aforementioned website, do not change our conclusion with the CSR solutions.

[25] Figure 9 shows the same as Figure 8 but around the other tropical region in Africa for the periods of the second half of March (a), the first half April (b), and the second half of April (c) in year 2005 and 6 months later depicted in (f) through (h). The maps shown in (d) and (e) is monthly mean water storage calculated from the global spherical harmonic coefficients in the month of April, 2005, with 500 km and 300 km smoothing, respectively. Figures 9i and 9j are the same as (d) and (e) but in the month of October, 2005. The dipole anomalies (positives in the southern part and negatives in the northern part) are reversed after 6 months due to the seasonal climate variability. Notably, the localized analysis yield stronger and more confined features implying significantly better spatial resolutions than the global analysis without leaking out the signals especially in the N-S direction.

[26] We also looked into North America including the Hudson Bay and the Mississippi basin. Figures 10a through (10c) are 15-day mass variation estimates (in terms of water height equivalent) from the first half of September in 2004

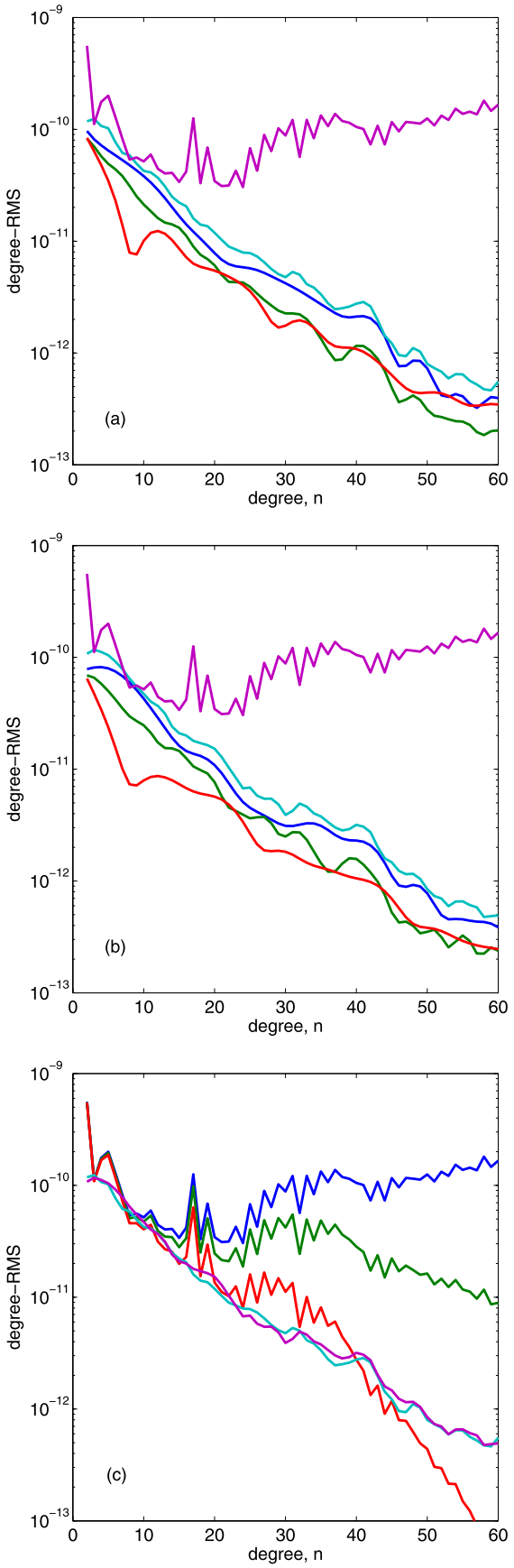

to first half of October in 2004. Figure 10d is from the monthly mean spherical harmonic coefficients on the month of September in 2004 with the smoothing radius of 500 km (300 km smoothing is too noisy and not shown here). From the localized solutions, we can see the positive anomalies are gradually disappearing in the southwest part of the Hudson Bay while the negative anomalies are being developed in the Rocky and Appalachian mountains. Figures 10e through (10h) are the same as (10a) through (10d) but one year later. The outstanding feature in the Hudson Bay and its surrounding area is inter-seasonal change which is as large as or larger than seasonal change. While the similar disappearance of the positive anomalies in the northern part is observed from the 15-day solutions in the year of 2005, the anomaly in the west of Hudson Bay has been significantly increased. Such inter-annual signal is believed to be partly due to hydrology and post-glacial rebound triggered by the retreat of the Laurentide ice sheet during the Pleistocene [*Peltier*, 2004].

[27] We calculate the power spectra of the localized solutions using the spherical harmonic coefficients computed by summing the equivalent water height estimates within the region up to the maximum spherical harmonic expansion degree of 60. Also see equations (31) and (32). The calculated coefficients essentially represent the spectra of the mass distribution on the sphere with zero outside the region of interest (the same effect as applying a window function on the global data, e.g., *Wieczorek and Simons* [2005]). Figures 11a and 11b show the degree-RMS (square root of the power spectra) of the monthly mean global solution in March 2005 and 15-day local solutions, first half of the month (a) and second half of the month (b), at South America, at Africa, and at North America. When those three local solutions are summed, it gives the degree-RMS closely following the power of the global solution within the degrees less than 15. The signal in South America is the strongest and the one in North America is the weakest among three of them. The power of the global solution is contaminated by the errors beyond the degrees greater than 15 or so. The growing power in the global solution after the degree 15 implies that the noise exceeds the signal. Figure 11c shows the degree-RMS of the summation of the three regional solutions and the degree-RMS of the global solutions without smoothing, 300 km smoothing, and 500 km smoothing. The 300 km smoothing seems to be

Figure 11. Degree-RMS (square root of degree-variance) of the 15-day regional solutions; (a) and (b) are the first and second half of March in 2005, respectively. The our regional solutions at South America (Blue), at Africa (Green) and at North America (Red) show less power than the monthly mean global harmonic solutions (Magenta), when the three solutions are summed (Cyan), the power is closer to the monthly mean solutions within the band less than degree 15. The errors in the global solution rapidly increase beyond the degree 15. The plot (c) compares the two 15-day regional solutions (Magenta and Cyan) with the power of the global spherical harmonic solutions without any smoothing (Blue) and with the smoothing of 300 km (Green) and 500 km (Red).

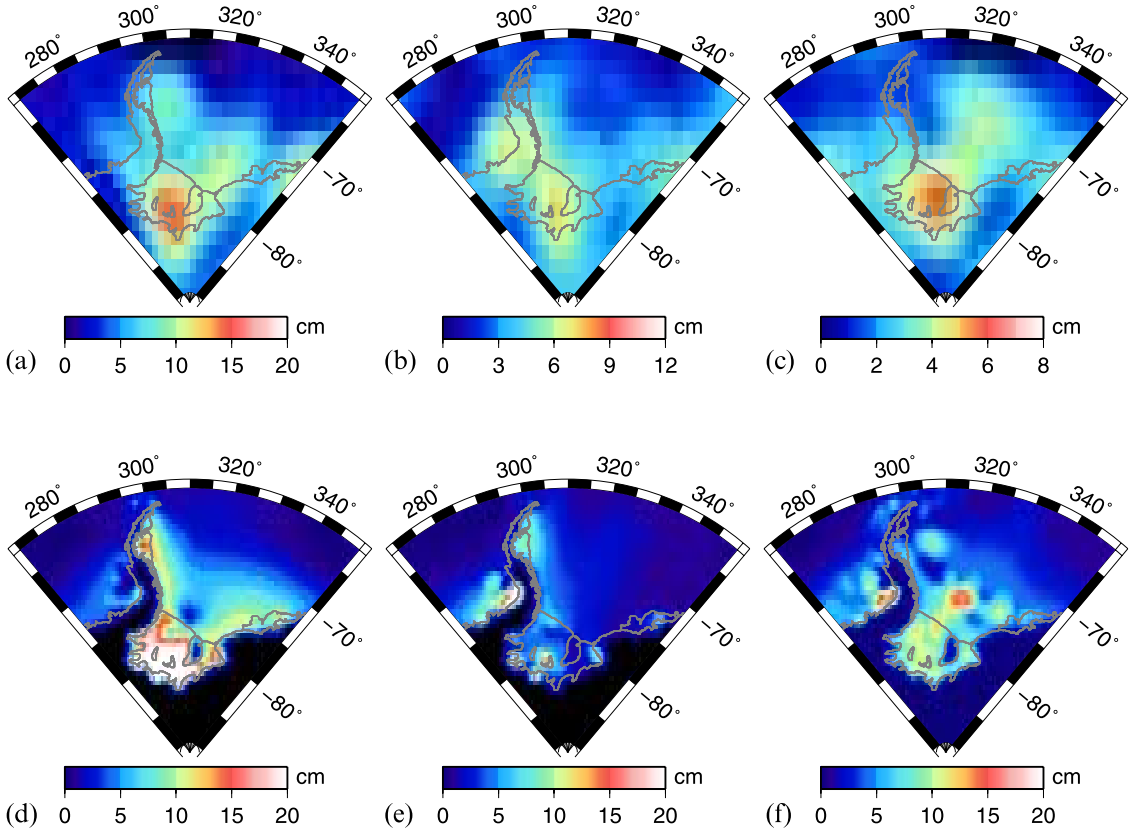

Figure 12. (a), (b), and (c) present the amplitudes of the residual M_2, S_2, and O_1 tides, respectively, in the Weddell Sea and Filchner-Ronne ice shelf, estimated by the localized analysis of 3 years of GRACE RRR observations. The residual tide indicates the anomaly with respect to the a priori model, GOT00. Note the various scale bars. (d), (e), and (f) show the amplitude of M_2, S_2, and O_1 tide from the model difference, GOT00−FES04. Note the GRACE estimates yield larger amplitude where the model difference is larger (or where the tide modeling is problematic).

still contaminated by significant amount of errors. However, we should note that the global analysis may not indicate the local variability of Signal-to-Noise Ratio (SNR). For example, Figures 8e and 8j with 300 km smoothing show the outstanding signal near the central Amazon and noise (not random but N-S elongated). The 500 km smoothing shown in Figures 8d and 8i actually filtered out the signal too much as well as noise. On the other hand, over Africa, the signal is not so outstanding compared to the noise when smoothed with 300 km (Figures 9e and 9j). It is due to the fact that the strength of the temporal gravity (mass) signal varies every region on the Earth. Such local variability of the temporal gravity signals in the global spherical harmonic coefficients can be quantified properly only after applying the localization before computing the global degree-variance as also discussed by *Han and Ditmar* [2007].

[28] The last example demonstrates another advantage from the local analysis of the satellite tracking data. We present the estimation of short-term (shorter than a day) periodic mass variations such as ocean tide anomaly. The majority of the ocean tide signal in the deep ocean at low and middle latitudes has been modeled out prior to analyzing the tracking data. However, the imperfect modeling yields tide anomalies localized mostly in the polar seas, ice shelves, and coastal areas. Those mass variations are periodic roughly with once-a-day and twice-a-day frequencies and significant only in certain regions. Depending on their original periods and the satellite sampling period, some of the constituents are largely canceled while some of them remain in the monthly gravity solutions [*Ray and Luthcke*, 2006]. The method developed in this study retrieves such mass variation signals and opens another new opportunity from the GRACE application. Using 3 years of RRR data, we estimated some of the constituents like M_2, S_2, and O_1 in the most problematic regions including the Filchner and Ross ice shelves (IS), Antarctica. The other major constituent K_1 is not estimable due to incomplete sampling of its phase in 3 years of period. We parameterize temporal variability on the basis of harmonic (sinusoidal) functions with seasonal frequency and tidal frequencies (only M_2, S_2, and O_1) and the functions for linear and offset, as explained in section 2.3. At this time, we do not solve the local gravity field at a fixed interval (like 15-days) but solve the respective coefficients of the modeled temporal functions directly from entire 3 years of RRR data. Figure 12 shows the amplitudes of M_2, S_2, and O_1 estimates from GRACE in (a), (b), and (c), respectively, and the amplitudes of the difference between two independent tide models, GOT00 [*Schrama and Ray*, 1994; *Ray*, 1999] and FES04 [*Lyard et al.*, 2006] for M_2, S_2, and O_1 in (d), (e), and (f),

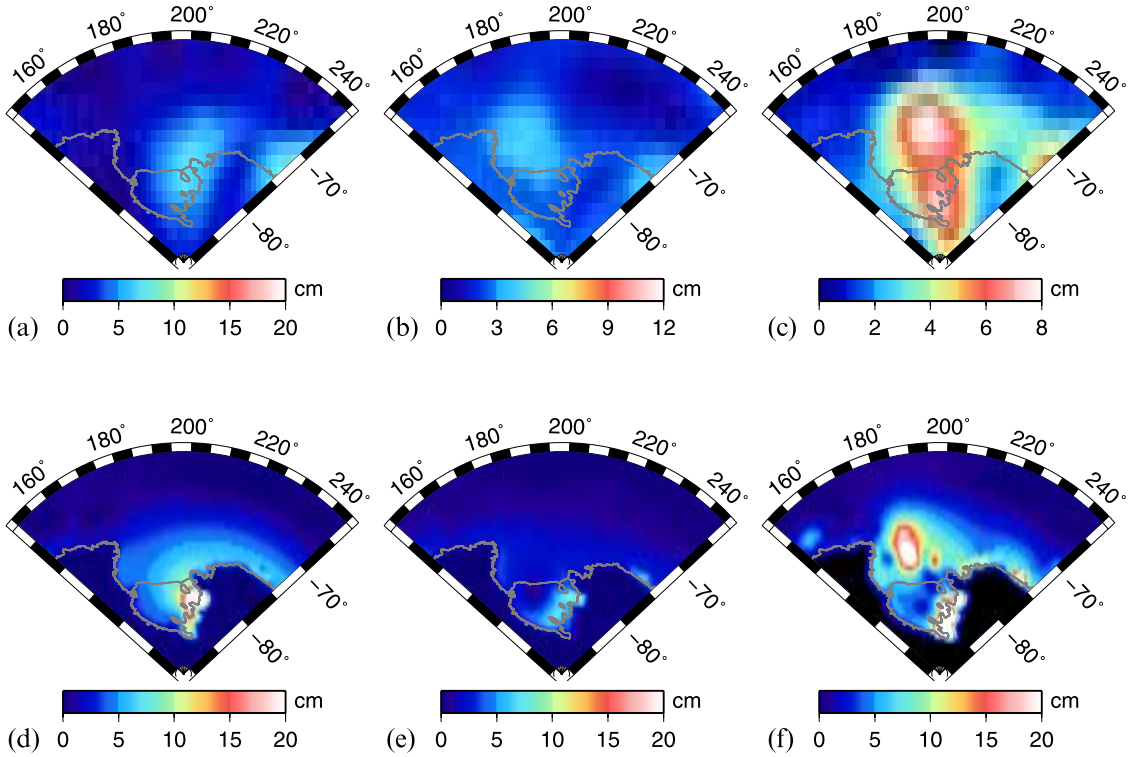

Figure 13. The same as Figure 11 but in the Ross Sea and Ross ice shelf. Note O_1 estimate is larger than the other two semi-diurnal tides in the Ross Sea, as also predicted by the model difference.

respectively. We applied the same temporal parameterization for all the mass points on land and ocean intentionally, while the point on the land obviously would not cause the variation at the tidal frequency (except the elastic loading near the coasts). The GRACE estimates provide the larger residual tides exactly where the model difference is larger; around Filchner IS for all three constituents, around Larsen IS for M_2, around Wilkins and Bach IS for S_2, and around Weddell Sea for O_1. The largest tidal anomaly is M_2 in this area, approaching 20 cm in amplitude near the grounding line of Filchner IS. Figure 13 shows the same but at the place including Ross IS and Ross Sea. In this region, GRACE predicts remaining M_2 tides near the grounding line of the Ross IS closer to the Rockefeller plateau. The most interesting anomaly in this region is largest residual O_1 tides in Ross Sea, approaching 8 cm in amplitude. *Han et al.* [2007] presents the comprehensive assessment of our GRACE tide estimates against available ground measurements surrounding the Antarctica continent.

4. Conclusion and Remark

[29] We explored a new way to analyze low-low satellite-to-satellite tracking data by numerically integrating the gravitational force from the mass anomalies on the surface within a certain area. The point mass approximation of the uniformly distributed surface mass within a block facilitates computation and yields modeling error that is not significant considering observational error as long as the size of the block is as reasonably small as 330^2 km^2. While the mass variation in the region generates a pulse-like pattern in the range-rate when integrated along the satellite orbits, the other signals and errors associated with mis-modeled and un-modeled forces (both gravitational and non-gravitational) and mass variations outside the region appear to be long-term trend in the over-flight range-rate residual observations. The simultaneous estimation of the mass parameter and incremental inter-satellite initial state is useful to retrieve the regional mass variation out of the noisy observations. The results from 3.5 years of GRACE data over South America, Africa, and North America show strong seasonal and inter-seasonal variability associated with regional hydrological mass and post-glacial rebound (only for North America) with greatly enhanced spatial and temporal resolutions clearly discerning sub-monthly variations. Another innovation was introduced by applying analytic functions for describing temporal variability of the gravity fields instead of estimating the gravity fields at a fixed interval. This kind of parameterization is demonstrated to be particularly useful to estimate even sub-daily mass variation such as tides. Global harmonic solutions cannot accommodate such characteristics in a dedicated manner, whereas regional solutions are better able to articulate the spatial and temporal characteristics and their mutual correlation. The regional solutions, taking advantage of the enhanced resolution and the localized mass transport characteristics, are expected to ultimately achieve an improved global model through a unified analysis of regional gravity patches in the future. Finally, the proposed method may help the community to study various science problems by analyzing the fundamental (satellite-tracking) data of the GRACE mission as well as the monthly geopotential products.

Appendix

[30] The inner-product between inter-satellite velocity and position vectors and the derivatives with respect to the mass anomaly vector and with respect to the incremental initial state vector difference are given as follows:

$$\begin{aligned}\mathbf{v}_{12}(t)^T\mathbf{r}_{12}(t) = {} & \tilde{\mathbf{v}}_{12}(t)^T\tilde{\mathbf{r}}_{12}(t) + \tilde{\mathbf{r}}_{12}(t)^T\delta\mathbf{v}_{12}^0 + \tilde{\mathbf{r}}_{12}(t)^T\mathbf{H}(t)\delta\mathbf{m} \\ & + \tilde{\mathbf{v}}_{12}(t)^T\delta\mathbf{r}_{12}^0 + \delta\mathbf{v}_{12}^{0^T}\delta\mathbf{r}_{12}^0 + \delta\mathbf{r}_{12}^{0^T}\mathbf{H}(t)\delta\mathbf{m} \\ & + \tilde{\mathbf{v}}_{12}(t)^T\mathbf{S}(t)\delta\mathbf{m}, + \delta\mathbf{v}_{12}^{0^T}\mathbf{S}(t)\delta\mathbf{m} \\ & + \delta\mathbf{m}^T\mathbf{H}(t)^T\mathbf{S}(t)\delta\mathbf{m} \end{aligned} \tag{A1}$$

and the derivatives are

$$\begin{aligned}\frac{\partial}{\partial\delta\mathbf{m}}\mathbf{v}_{12}(t)^T\mathbf{r}_{12}(t) = {} & \mathbf{H}(t)^T\tilde{\mathbf{r}}_{12}(t) + \mathbf{H}(t)^T\delta\mathbf{r}_{12}^0 + \mathbf{H}(t)^T\mathbf{S}(t)\delta\mathbf{m} \\ & + \mathbf{S}(t)^T\tilde{\mathbf{v}}_{12}(t) + \mathbf{S}(t)^T\delta\mathbf{v}_{12}^0 + \mathbf{S}(t)^T\mathbf{H}(t)\delta\mathbf{m}, \\ & = \mathbf{H}(t)^T\mathbf{r}_{12}(t) + \mathbf{S}(t)^T\mathbf{v}_{12}(t) \end{aligned} \tag{A2}$$

$$\frac{\partial}{\partial\delta\mathbf{r}_{12}^0}\mathbf{v}_{12}(t)^T\mathbf{r}_{12}(t) = \tilde{\mathbf{v}}_{12}(t) + \delta\mathbf{v}_{12}^0 + \mathbf{H}(t)\delta\mathbf{m} = \mathbf{v}_{12}(t), \tag{A3}$$

$$\frac{\partial}{\partial\delta\mathbf{v}_{12}^0}\mathbf{v}_{12}(t)^T\mathbf{r}_{12}(t) = \tilde{\mathbf{r}}_{12}(t) + \delta\mathbf{v}_{12}^0 + \mathbf{S}(t)\delta\mathbf{m} = \mathbf{r}_{12}(t). \tag{A4}$$

The following inner-product between the inter-satellite position vectors and the derivatives with respect to the mass anomaly vector and with respect to the incremental initial state vector difference are expressed as follows:

$$\begin{aligned}\mathbf{r}_{12}(t)^T\mathbf{r}_{12}(t) = {} & \tilde{\mathbf{r}}_{12}(t)^T\tilde{\mathbf{r}}_{12}(t) + \tilde{\mathbf{r}}_{12}(t)^T\delta\mathbf{r}_{12}^0 + \tilde{\mathbf{r}}_{12}(t)^T\mathbf{S}(t)\delta\mathbf{m} \\ & + \tilde{\mathbf{r}}_{12}(t)^T\delta\mathbf{r}_{12}^0 + \delta\mathbf{r}_{12}^{0^T}\delta\mathbf{r}_{12}^0 + \delta\mathbf{r}_{12}^{0^T}\mathbf{S}(t)\delta\mathbf{m} \\ & + \tilde{\mathbf{r}}_{12}(t)^T\mathbf{S}(t)\delta\mathbf{m} + \delta\mathbf{r}_{12}^{0^T}\mathbf{S}(t)\delta\mathbf{m} \\ & + \delta\mathbf{m}^T\mathbf{S}(t)^T\mathbf{S}(t)\delta\mathbf{m}, \end{aligned} \tag{A5}$$

and the derivatives are given by

$$\frac{\partial}{\partial\delta\mathbf{m}}\mathbf{r}_{12}(t)^T\mathbf{r}_{12}(t) = 2\mathbf{S}(t)^T\mathbf{r}_{12}(t), \tag{A6}$$

$$\frac{\partial}{\partial\delta\mathbf{r}_{12}^0}\mathbf{r}_{12}(t)^T\mathbf{r}_{12}(t) = 2\mathbf{r}_{12}(t), \tag{A7}$$

$$\frac{\partial}{\partial\delta\mathbf{v}_{12}^0}\mathbf{r}_{12}(t)^T\mathbf{r}_{12}(t) = 0, \tag{A8}$$

[31] **Acknowledgments.** This work was partially supported by the U.S. National Aeronautical and Space Administration Earth Surface and Interior program and Gravity Recovery and Climate Experiment project. We acknowledge the NASA/GFZ GRACE project for the GRACE data products (distributed by JPL PODAAC). We acknowledge colleagues at JPL for producing the high-quality Level-1B GRACE products. We thank Richard Ray for valuable discussion. The associate editor, Pavel Ditmar, and an anonymous reviewer are acknowledged for their help to improve the manuscript.

References

Bettadpur, S. (2004), Level−2 Gravity Field Product User Handbook, GRACE, pp. 327−734, Jet Propul. Lab., Pasadena, Calif.

Chambers, D., J. Wahr, and R. Nerem (2004), Preliminary observations of global ocean mass with GRACE, *Geophys. Res. Lett.*, *31*, L13310, doi:10.1029/2004GL020461.

Chao, B. F., W. P. O'Connor, A. T. C. Chang, D. K. Hall, and J. L. Foster (1987), Snow load effects on the Earth's rotation and gravitational field, 1979−1985, *J. Geophys. Res.*, *92*(B9), 9415−9422.

Chao, B. F., and A. Au (1991), Temporal variation of the Earth's low-degree field caused by atmospheric mass distribution- 1980-1988, *J. Geophys. Res.*, *96*(B4), 6569−6575.

Davis, J. L., P. Elosegui, J. X. Mitrovica, and M. E. Tamisiea (2004), Climate-driven deformation of the solid Earth from GRACE and GPS, *Geophys. Res. Lett.*, *31*, L24605, doi:10.1029/2004GL021435.

Han, D., and J. Wahr (1995), The viscoelastic relaxation of a realistically stratified Earth, and a further analysis of post glacial rebound, *Geophys. J. Int.*, *120*, 287−311.

Han, S.-C., C. Jekeli, and C. K. Shum (2004), Time-variable aliasing effects of ocean tides, atmosphere, and continental water mass on monthly mean GRACE gravity field, *J. Geophys. Res.*, *109*, B04403, doi:10.1029/2003JB002501.

Han, S.-C., C. K. Shum, C. Jekeli, C.-Y. Kuo, C. Wilson, and K.-W. Seo (2005a), Non-isotropic filtering of GRACE temporal gravity for geophysical signal enhancement, *Geophys. J. Int.*, *163*, 18−25, doi:10.1111/j.1365-246X.2005.02756.x.

Han, S.-C., C. K. Shum, C. Jekeli, and D. Alsdorf (2005b), Improved estimation of continental water storage change from GRACE, *Geophys. Res. Lett.*, *32*, L07302, doi:10.1029/2005GL022382.

Han, S.-C., and P. Ditmar (2007), Localized spectral analysis of global satellite gravity fields for recovering time-variable mass redistribution, *J. Geod.*, doi:10.1007/s00190-007-0194-5, in press.

Han, S.-C., R. D. Ray, and S. B. Luthcke (2007), Ocean tidal solutions in Antarctica from GRACE inter-satellite tracking data, *Geophys. Res. Lett.*, *34*, L21607, doi:10.1029/2007GL031540.

Heiskanen, W., and H. Moritz (1967), *Physical Geodesy*, Freeman, San Francisco, Calif.

IERS, IERS Conventions (2003), IERS Technical Note 32, edited by D. McCarthy and G. Petit, Frankfurt am Main: Verlag des Bundesamts für Kartographie und Geodäsie.

Koch, K.-R., and J. Kusche (2002), Regularization of geopotential determination from satellite data by variance components, *J. Geod.*, *76*, 259−268.

Luthcke, S. B., D. D. Rowlands, F. G. Lemoine, S. M. Klosko, D. Chinn, and J. J. McCarthy (2006), Monthly spherical harmonic gravity field solutions determined from GRACE inter-satellite range-rate data alone, *Geophys. Res. Lett.*, *33*, L02402, doi:10.1029/2005GL024846.

Lyard, F., F. Lefèvre, T. Letellier, and O. Francis (2006), Modelling the global ocean tides: Insights from FES2004, *Ocean Dyn.*, *56*, 394−415.

Mayer-Gürr, T., A. Eicker, and K. H. Ilk (2006), Gravity Field Recovery from GRACE-SST Data of Short Arcs, in *Observation of the Earth System from Space*, edited by J. Flury et al., pp. 131−148, Springer, Berlin.

Paul, M. K. (1978), Recurrence relations for integrals of associated Legendre functions, *Bull. Geod.*, *52*, 177−190.

Pavlis, D. E., S. Poulose, and J. J. McCarthy (2006), GEODYN Operations Manuals, SGT Inc., Greenbelt, Md.

Peltier, W. R. (2004), Global glacial isostasy and the surface of the ice-age Earth: The ICE-5G (VM2) model and GRACE, invited paper, *Annu. Rev. Earth Planet. Sci.*, *32*, 111−149.

Petrov, L., and J.-P. Boy (2004), Study of the atmospheric pressure loading signal in very long baseline interferometry observations, *J. Geophys. Res.*, *109*, B03405, doi:10.1029/2003JB002500.

Ray, R. D. (1999), A global ocean tide model from TOPEX/POSEIDON altimetry: GOT99.2, NASA Tech. Memo., 1999-209478, Goddard Space Flight Center, Greenbelt, Md.

Ray, R. D., and S. B. Luthcke (2006), Tide model errors and GRACE gravimetry: Towards a more realistic assessment, *Geophys. J. Int.*, *167*(3), 1055−1059, doi:10.1111/j.1365-246X.2006.03229.x.

Ray, R. D., and R. M. Ponte (2003), Barometric tides from ECMWF operational analyses, *Ann. Geophys.*, *21*, 1897−1910.

Rowlands, D. D., R. D. Ray, D. S. Chinn, and F. G. Lemoine (2002), Short-arc analysis of intersatellite tracking data in a gravity mapping mission, *J. Geod.*, *76*, 307−316.

Rowlands, D., S. Luthcke, S. Klosko, F. Lemoine, D. Chinn, J. McCarthy, C. Cox, and O. Anderson (2005), Resolving mass flux at high spatial and temporal resolution using GRACE intersatellite measurements, *Geophys. Res. Lett.*, *32*, L04310, doi:10.1029/2004GL021908.

Schrama, E. J. O., and R. D. Ray (1994), A preliminary tidal analysis of Topex/Poseidon altimetry, *J. Geophys. Res.*, *99*(C12), 24,799−24,808.

Swenson, S., and J. Wahr (2006), Post-processing removal of correlated errors in GRACE data, *Geophys. Res. Lett.*, *33*, L08402, doi:10.1029/2005GL025285.

Tapley, B. D., S. Bettadpur, J. Ries, P. Thompson, and M. Watkins (2004a), GRACE measurements of mass variability in the Earth system, *Science*, *305*, 503–505.

Tapley, B. D., S. Bettadpur, M. Watkins, and Ch. Reigber (2004b), The Gravity Recovery and Climate Experiment; Mission overview and early results, *Geophys. Res. Lett.*, *31*(9), L09607, doi:10.1029/2004GL019920.

Tapley, B. D., et al. (2005), GGM02 - An improved Earth gravity field model from GRACE, *Geod. J.*, *79*, 467–478, doi:10.1007/s00190-005-0480-z.

Velicogna, I., and J. Wahr (2006), Measurements of time-variable gravity show mass loss in Antarctica, *Science*, *311*, 1754–1756.

Wagner, C., D. McAdoo, J. Klokocnik, and J. Kostelecky (2006), Degradation of geopotential recovery from short repeat-cycle orbits: Application to GRACE monthly fields, *J. Geod.*, *80*, 94–103.

Wahr, J., F. Molenaar, and F. Bryan (1998), Time variability of the Earth's gravity field: Hydrological and oceanic effects and their possible detection using GRACE, *J. Geophys. Res.*, *103*(B12), 30,205–30,229.

Wieczorek, M. A., and F. J. Simons (2005), Localized spectral analysis on the sphere, *Geophys. J. Int.*, *162*, 655–675, doi:10.1111/j.1365-246X.2005.02687.x.

Zlotnicki, V., J. Wahr, I. Fukumori, and Y. Song (2007), Antarctic circumpolar current transport variability during 2003-05 from GRACE, *J. Phys. Oceanogr.*, *37*, 230–244.

S.-C. Han, F. G. Lemoine, S. B. Luthcke, and D. D. Rowlands, Planetary Geodynamics Laboratory, Code 698, NASA Goddard Space Flight Center, 8800 Greenbelt Road, Greenbelt, MD 20771, USA. (schan@puuoo.gsfc.nasa.gov)